



LAWRENCE
LIVERMORE
NATIONAL
LABORATORY

Unusual lithiation and fracture behavior of silicon mesoscale pillars: roles of ultrathin atomic layer coatings and initial geometry

J. C. Ye, Y. H. An, M. M. Biener, R. J. Nikolic, M. Tang, H. Q. Jiang, Y. M. Wang

July 3, 2013

Journal of Power Sources

Disclaimer

This document was prepared as an account of work sponsored by an agency of the United States government. Neither the United States government nor Lawrence Livermore National Security, LLC, nor any of their employees makes any warranty, expressed or implied, or assumes any legal liability or responsibility for the accuracy, completeness, or usefulness of any information, apparatus, product, or process disclosed, or represents that its use would not infringe privately owned rights. Reference herein to any specific commercial product, process, or service by trade name, trademark, manufacturer, or otherwise does not necessarily constitute or imply its endorsement, recommendation, or favoring by the United States government or Lawrence Livermore National Security, LLC. The views and opinions of authors expressed herein do not necessarily state or reflect those of the United States government or Lawrence Livermore National Security, LLC, and shall not be used for advertising or product endorsement purposes.

DOI: 10.1002/aenm.((please add manuscript number))

Article type: full paper

Unusual lithiation and fracture behavior of silicon mesoscale pillars: roles of ultrathin atomic layer coatings and initial geometry

*Jianchao Ye, Yonghao An, Monika M. Biener, Rebecca J. Nikolic, Ming Tang, Hanqing Jiang, Y. Morris Wang**

Dr. J.C. Ye, Y.H. An, Dr. M.M. Biener, Dr. M. Tang, Dr. Y.M. Wang^{*}

Physical and Life Sciences Directorate, Lawrence Livermore National Laboratory, Livermore, CA 94550, USA

Email: ymwang@llnl.gov

Dr. R.J. Nikolic

Center for Micro and Nano Technology, Lawrence Livermore National Laboratory, Livermore, CA 94550, USA

Y.H. An, Prof. H. Jiang

School for Engineering of Matter Transport and Energy, Arizona State University, Tempe, AZ 85287, USA

Keywords: silicon micropillars, atomic layer deposition, TiO₂, Al₂O₃, solid electrolyte interphase

Abstract

Crystalline silicon nanostructures are commonly known to exhibit anisotropic expansion behavior during the lithiation that leads to grooving and fracture. Strategies such as surface coatings have been hitherto developed to tackle these problems in order to enhance the cycling life of silicon when applied as anodes for lithium ion batteries. Here we report surprisingly relatively uniform expansion behavior of (100) single crystalline silicon micropillars (~2 μm) during the initial lithiation, which only become strongly anisotropic after atomic layer deposition of ultrathin metal oxide coatings. The results suggest that the formation of solid-electrolyte interphases play a critical role in regulating lithium ion transport and subsequent volume expansion behavior. We systematically explore the ultrathin coating effects on the anisotropic volume expansion, fracture patterns, and stress evolutions. Models are developed to address rather complex fracture behavior seen in several types of pillars. We find that both thin surface coatings and square geometry substantially suppress fracture development and enhance volume expansion, albeit with distinctively different mechanisms. These findings caution a random extrapolation of observations in nanostructure silicon and shed lights on the future design of this material for high-performance lithium ion battery applications.

1. Introduction

The large lithium storage capacity (~ 3579 mAh/g in theory) and industry scalable manufacturing capability of various silicon materials have inspired intense research in these materials as anodes for lithium-ion batteries (LIB).^[1, 2] The enormous potential of silicon as energy storage materials has however been counteracted by several known challenges, including a rather large volume expansion (VE $\sim 300\%$) during lithiation that inevitably degrades the structural integrity of silicon electrodes during the cycling, highly anisotropic lithiation/delithiation behavior witnessed in single crystalline silicon, and poor solid electrolyte interphase (SEI) layer formation. To overcome the first two shortcomings, a wide variety of nanostructures or amorphous silicon (e.g., nanowires, nanotubes, nanoparticles, and nanoporous structures) have been intensively investigated where much valuable information has been garnered.^[3-9] Unfortunately nanostructured silicon is expensive to scale-up and also suffer from intrinsically low tapped density (leading to low volumetric capacity). In comparison, the electrochemical and electromechanical behavior of mesoscale (e.g., micrometer-sized) silicon is less well understood. To date only a handful of experiments have been conducted.^[10, 11] Because of the clear size, stress and subsequent phase boundary curvature differences, the lithiation kinetics of micro-sized silicon is expected to be quite different from that of nanostructures. Such information could nonetheless bear critical relevance to the commercial applications due to the high energy density needs that call for thick electrodes (e.g., commercial electrodes are typically over 100 micrometers thick).

Another critical challenge yet little understood to the long cycle life of silicon-based LIBs is to overcome the poor SEI layers that are intrinsically associated with large volume change electrodes. Such SEI layers are unstable both mechanically and thermally as the SEI layer is an organic/inorganic composite (e.g., containing Li_2CO_3 , LiF , $(\text{CH}_2\text{OCO}_2\text{Li})_2$, polycarbonates)^[12] that could decompose at a relatively low temperature. The continuous re-

exposure of fresh silicon to electrolyte due to the instability of SEI leads to low Coulombic efficiency and may promote subsequent exothermal reactions that lead to “thermal runaway” and cause fire and explosion of LIBs due to the chain reactions of oxidative cathode materials (if a full cell configuration is used). As such, the thermal and mechanical stability of SEI layers on anodes is also of importance to the safety of LIBs. To this end, few studies have been performed to address these SEI issues, with existing effort focused on carbon or silicon oxide coatings as the potential front-runner solutions. The former is electrically conductive such that it may not be able to impede the growth of SEI at low potentials,^[11] while the latter has low fracture toughness [see [Supporting Information \(SI\), Table S1](#)] and can be reactive to fluoride species, and thus requires strict structural designs.^[1] Another important class of coating materials are metal oxides, which can not only offer high thermal stability, but also possess other beneficial properties such as high mechanical strength and fracture toughness, low electrical conductivity, and high lithium diffusivity ([SI, Table S1](#)). These unique properties render them as excellent surface protection materials for anodes (as well as cathodes). Enhanced cycling performance and high Coulombic efficiency have indeed been reported in Al₂O₃-coated silicon nanostructures.^[13, 14] Nonetheless, there exists limited understanding of the impact of metal oxide coatings on the lithiation and fracture/failure behavior of silicon materials.

By using atomic layer deposition (ALD), here we report on the surprising lithiation and fracture behavior of silicon micropillar arrays that are ALD-ed with an ultrathin layer (<1 nm) of Al₂O₃ and TiO₂, respectively. Silicon micropillars for this study were directly fabricated from (100) n-type silicon wafers with a diameter of 2 μm and a height of 50 μm, yielding a height/diameter aspect ratio of 25:1 (see Experimental Section). To our knowledge, this is the highest aspect ratio silicon micropillars reported so far for investigation of lithiation behavior, which mechanistically ensures plane strain condition near the pillar top without having to take

into account the substrate confinement effect. Similar pillars have been popularly used as thermal neutron detector materials with excellent performance.^[15] The penetration ability of ALD technique to very high aspect ratio structures further makes these studies possible. We investigate two types of conformal coatings; i.e., 0.75 nm thick Al_2O_3 and 1 nm thick TiO_2 , respectively. To explore the initial pillar geometry effect on the lithiation/fracture behavior, square micropillars were also fabricated. Systematic and comparison experiments were performed on the bare silicon circular micropillars (bare-Circular-Si), Al_2O_3 -coated (Al_2O_3 -ALD-Circular-Si) and TiO_2 -coated (TiO_2 -ALD-Circular-Si) silicon circular micropillars, and TiO_2 -coated square micropillars (TiO_2 -ALD-Square-Si). For the square-shaped pillars, the orientation of four sides is oriented along $\{110\}$ crystallographic planes, which is considered as the fastest Li diffusion direction in silicon. The high quality and well-patterned nature of all as-fabricated pillars can be seen in Fig. 1a-c scanning electron microscopic (SEM) images. Earlier studies have generally revealed that circular shape nanowires exhibit strong anisotropic expansion, leading to grooving and fracture. It is thus interesting and of technological importance whether similar behavior occurs in mesoscale pillars and whether one can take advantage of geometrical design to mitigate or even completely annihilate such anisotropic failure behavior.

2. Results and discussion

Unexpected lithiation behavior before and after ALD. With a half-cell configuration shown in Fig. 1d, we investigated the initial lithiation behavior of above silicon micropillars, including Li uptake, SEI formation, VE, and fracture behavior. The lithiation time for all pillars is fixed at 20 hrs (see Experimental Section), and the total Li uptake is estimated from the current profile for three types of circular pillars, as illustrated in Fig. 1e. In our calculations, we simply count the weight of silicon micropillars, as the lithiation of substrate accounts for <5% of total Li intake based on the surface area of the substrate. Interestingly,

the apparent lithiation intake of bare Si reached up to 8.8 Li per Si after 20 hrs of lithiation, which is well above the theoretical Li storage capacity (3.75 Li per Si by assuming $\text{Li}_{15}\text{Si}_4$ room-temperature product). This suggests the formation of massive SEI layers under the current low-voltage lithiation conditions (i.e., 50 mV). This behavior is confirmed by SEM images shown in Fig. 2a, where the SEI layer is rather rough for the bare silicon, and can be up to $\sim 0.5\text{-}0.8\ \mu\text{m}$ thick (SI, Fig. S1). In contrast, such SEI formation has been substantially mitigated in both Al_2O_3 -coated and TiO_2 -coated samples, Fig. 2b and Fig. 2c, respectively. Quantitative measurements from the cross-section of micropillars using focused-ion-beam cutting suggest that the thickness of SEI layers in ALD-coated samples is no more than 150 nm (SI, Figs. S2, S3). Unexpectedly, we observe relatively uniform VE behavior for the bare-Circular-Si before the fracture (Fig. 2a and SI, Fig. S1), in contrast to widely reported anisotropic expansion of silicon crystalline nanowires or nanopillars.^[3] In our cases, strong anisotropic VE is only observed for ALD-coated samples (Fig. 2b and 2c). The near uniform expansion behavior seen in the bare-Circular-Si suggests that the formation of SEI layers plays a crucial role in regulating lithium transport under our current experimental conditions, and that the lithiation behavior of these bare-Circular-Si micropillars may no longer be controlled by the phase-boundary mobility.^[2] To quantify the anisotropic VE behavior in three types of samples, we define an anisotropic index factor χ as the ratio of pillar dimension along the $\langle 110 \rangle$ ($d_{\langle 110 \rangle}$, preferentially swelling direction) and $\langle 100 \rangle$ direction ($d_{\langle 100 \rangle}$, least expansion direction) right before the crack formation. Table 1 indicates that the bare-Circular-Si has a χ value of 1.02 ± 0.03 (i.e., near uniform expansion), approximately 13% smaller compared to the values of Al_2O_3 -ALD-Circular-Si ($\chi = 1.15 \pm 0.03$) and TiO_2 -ALD-Circular-Si ($\chi = 1.13 \pm 0.04$) pillars. Moreover, we find that the overall achievable VE before fracture of both ALD-samples is about 10% higher than that of the bare-Circular-Si, suggesting the positive role of ALD coatings. The present experimental results indicate that, due to the

excellent ionic conductivity but electronically insulating nature of metal oxides (SI, Table S1), these ultrathin ALD coatings not only help to form and stabilize thin SEI layers (leakage of electrons is one of the main causes that promote the decomposition of electrolytes), but also enhance the VE of silicon micropillars (likely due to the suppression of surface defects after ALD, to be discussed later).

Square pillars vs. circular pillars (geometry effect). Compared to circular pillars, the VE behavior of square pillars is quite intriguing. For meaningful comparison, we also ALD-ed square pillars with the same thickness of TiO_2 and carried out lithiation experiments under the same conditions as those of circular pillars. Interestingly, the square pillars become near circular shape after lithiation due to the preferential expansion of $\{110\}$ side surface, Fig. 2d. As a result, the χ value increases from 0.71 (square) to 0.95 ± 0.02 (close to circular shape) after lithiation. Significantly, the overall VE of square pillars increases up to 165% before cracks initiate; this represents an impressive 88% increment over the circular pillars, Table 1. These results strongly argue that square shape (instead of circular one) is a better geometry for large Li storage in silicon – an interesting observation that has not been reported in the literature.

Fracture behavior. It is noted in Fig. 2a-c and SI, Fig. S4 that all silicon pillars exhibit popcorn type fracture patterns, where cracks appear to initiate from the surface of circular pillars, penetrating into the crystalline core and also propagating along the crystalline-amorphous interfaces. In addition, all pillars (including square ones) seem to fail from one major crack rather than multiple ones. To obtain more quantitative information, we have measured the crack orientations of all four types of silicon pillars. Fig. 3 illustrates the statistical crack orientation information for the bare-Circular-Si, ALD circular pillars (both), and TiO_2 -ALD-square-Si. Due to the relatively uniform expansion behavior of the bare-Circular-Si, we observe that the crack orientation of these samples is somewhat stochastic

with slight preference along $\langle 110 \rangle$ direction, Fig. 3a; i.e., the reported preferential fracture oriented 45° to $\langle 110 \rangle$ direction for (100)-type silicon nanopillars is not observed in our micropillars.^[3] For ALD circular pillars, cracks seem to initiate unanimously along $\langle 110 \rangle$ direction (i.e., the most swelling direction), Fig. 2b, whereas for ALD square pillars, along $\langle 100 \rangle$ direction (i.e., one corner of the square), Fig. 2c. These fracture orientations are not only drastically different from those of our own bare silicon, but also differ from dominant fracture orientations reported so far in the literature,^[3] suggesting that the fracture process in silicon micropillars can be quite a complex, which seems affected by the sample size, initial geometry, surface coatings/defects, or even dopant type. In addition, different electrochemical reaction rate used in various experiments could also play a significant role. Note that the different fracture orientations reported in the literature are mainly observed in p-type silicon nanopillars,^[3] whereas our samples are n-type pillars. Furthermore, there are clear sample size and lithiation condition differences. The experimental results here underscore the importance of taking into account the strong size effect, initial sample geometry, and electrochemical cycling conditions when designing silicon anode structures for LIBs.

To further grip the crack growth trends for all four types of pillars studied, we measured the crack length (L) (defined in Fig. 4a, where R is the original radius of the pillar) vs. VE for a number of randomly selected pillars. The results are summarized in Fig. 4b for all pillars. In the figure, one could gauge the easiness of the crack propagation through examining the slope (K) of L/R vs. VE. A larger K would mean that the crack is prone to propagation under the same VE. We note that, for the bare silicon, the cracks always nucleate from the out surface after a VE of less than 100% and start to grow inwards with a K value of ~ 2.7 . Both ALD-coated samples follow a similar trend ($K \sim 2.3$) but with a slightly larger x-axis offset compared to the bare silicon, suggesting that ALD coating might have helped to arrest the crack nucleation. We speculate that as our coating thickness is no more than 1 nm (i.e.,

negligibly thin compared to the sample dimension), the possible mechanical constraint effect is insignificant. This is consistent with similar K values observed for all three circular shaped samples. As mentioned above and indicated in Fig. 4b, the ALD-square pillars reveal a critical VE of 165% that is much larger than the circular ones. This implies a strong delay of crack nucleation and propagation. In addition, we find a K value of ~1.5 for these square pillars, which is also substantially smaller than those of circular ones (2.3-2.7), testifying more difficult event of crack propagation in the square pillars. Based upon the critical VE without fracture (ΔV_c), one can estimate a reversible capacity of ~2300 mAh/g for ALD square pillars, in contrast to a much smaller capacity of ~1400 mAh/g for circular pillars.

Another important question pertaining to the crack propagation is whether the two phase boundary can effectively divert or obstruct the crack propagation. If this occurs, one would expect to see the crack length (L) equal or be smaller than the amorphous shell thickness (t; i.e., lithiated area). Assuming an isotropic VE (ΔV), one can estimate t/R from the total ΔV as:

$$t / R = \sqrt{1 + \Delta V} - \sqrt{1 - \Delta V / \Delta V_t} , \quad (1)$$

where ΔV_t represents the theoretical VE of silicon. The calculated t/R trend follows the dashed line shown in Fig. 4b. Evidently, L/R values surpass the t/R line for all three circular pillars when the VE is above ~100%, suggesting that the cracks propagate well into the crystalline silicon core for circular pillars, consistent with the SEM image shown in Fig. 4a. In contrast, this behavior is not seen for square pillars, which again suggests the difficult event of crack propagation in square geometry. The contrast results between circular and square pillars promote us to argue that the stress state/distribution in these two types of pillars could be very different.

3. Modeling

To further help understand very different fracture behavior observed before and after ALD coatings, and the strong sample geometry effect observed in our work, we carried out

finite element modeling (FEM) using an ABAQUS package. The details of model setup and the selection of physical parameters can be seen in the modeling details. Note that earlier in-situ transmission electron microscopy experiments revealed a strong orientation-dependent interface mobility during lithiation of silicon nanowires,^[2, 16] which has been the basis of many existing modeling effort.^[16, 17] Our experiments here on the bare silicon pillars however indicate that the lithiation behavior of silicon materials is strongly influenced by the formation of SEI layers, which regulates/limits the lithium ion transport such that the interface mobility could become less relevant. In fact and as indicated by the modeling results shown in Fig. 5a-d, a relatively uniform VE behavior is obtained when the interface velocity difference is less than 10% along the $\langle 110 \rangle$ and $\langle 100 \rangle$ directions; i.e., the rate controlling mechanism in our bare silicon micropillars is likely to be the diffusion of lithium ion into the reaction front. Under these conditions, our simulations indicate that the corresponding hoop stresses (Fig. 5a) along $\langle 110 \rangle$ (σ_{110}) and $\langle 100 \rangle$ (σ_{100}) directions are initially compressive but quickly turn over to the positive territory (i.e., tensile). Right before the fracture (i.e., at the VE ~82%), both stresses are clearly tensile and exhibit essentially the same values. These results agree quantitatively with relatively stochastic fracture orientations of bare silicon micropillars observed in our experiments. In contrast, an obviously anisotropic VE behavior is duplicated when the interface mobility is assumed to control the VE behavior of ALD samples, Fig. 5e-h. Under this scenario, the hoop stresses go through a similar transition from compressive to tensile with the major difference that the hoop stress along $\langle 110 \rangle$ direction (i.e., σ_{110}) is appreciably higher than σ_{100} , leading to preferential fracture of these pillars long $\langle 110 \rangle$ orientation (as observed in our experiments). The similar magnitude of overall hoop stresses in bare and ALD samples suggest that the constraint effect of ultrathin coatings is negligible – an outcome that is in line with the experimental observations.

Interestingly, the round shape expansion behavior of ALD square pillars is also reproduced when interfacial mobility is assumed to control the lithiation behavior of these pillars, the hoop stresses of which exhibit a cross-over behavior between $\langle 100 \rangle$ and $\langle 110 \rangle$ orientations. The hoop stress along $\langle 100 \rangle$ orientation is observed to be higher when the VE is less than $\sim 125\%$, which is gradually overtaken by the stress along $\langle 110 \rangle$ direction. The gradual decrease of σ_{100} as VE increases is observed to be linked with the stress relaxation along the corner of the square (Fig. 5i), suggesting that the square pillars has the ability to homogenize the stress distribution and slow down the crack nucleation or growth. The final fracture of these pillars along $\langle 100 \rangle$ direction seems pertaining to the groove development observed in our simulations, Fig. 5j-l. Note that the fracture toughness in bulk silicon is orientation dependent, with the value along $\langle 110 \rangle$ direction slightly lower than that of $\langle 100 \rangle$ direction (SI, Table S1). This small fracture toughness discrepancy however does not seem to affect the fracture orientation of square pillars. The rather complex stress evolution and much larger achievable VE in these pillars suggest that square geometry is more desirable for applications in LIBs. It is further suggested that investigations of other geometry pillars are useful in order to fully understand the initial geometric effect of silicon crystalline materials upon lithiation behavior. Despite the relative simplicity of the modeling approach, our simulations here are able to catch the essences of shape change of all three types of pillars, as well as the fracture orientations. We observe different rate controlling mechanisms in bare and ALD pillars, with very different hoop stress development that is closely related to the shape of the pillars.

4. Summary and conclusions

In summary, we have investigated the initial lithiation behavior of (100) n-type silicon micropillars in three different forms: bare circular silicon, ALD-coated circular silicon, and ALD-coated square silicon pillars. In contrast to what has been reported in the literature on

nanostructures, the bare silicon micropillars studied here exhibit a relatively uniform VE behavior before fracturing along somewhat stochastic directions, likely due to the regulation effect of SEI layers in controlling lithium ion flux. ALD coating of metal oxides (Al_2O_3 and TiO_2) help to form thin SEI layers and enhance lithium transportation, leading to a strong anisotropic VE behavior. With or without ALD coatings, the critical VE before fracture for all circular pillars reaches up to $\sim 100\%$. With a further square-shaped geometry design, however, a critical VE of more than 165% can be reached, helped by the stress relaxation mechanisms around the corners of squares. Models are developed that are able to rationalize the overall VE and fracture behavior of all pillars. Simulations further suggest that stress distributions in various pillars may play significant roles in the fracture behavior. These findings stress a strong size-dependent fracture behavior in crystalline silicon, and offer new insights in designing silicon-based electrodes for high energy density and high-power density electrochemical energy storage.

Experimental Section

Preparation of Si micropillars: Bulk n-type (100) silicon wafers with the conductivity of 2 S/cm (determined by a 4 point probe) were selected for micropillar fabrication. The pillar diameter and spacing were defined lithographically, followed by inductively coupled plasma etching to form the pillar arrays. The etch process used a Bosch Process also known as pulsed or time-multiplexed etching, alternating repeatedly between two modes to achieve nearly vertical structures. This was completely by alternating between using a plasma to isotropically etch the silicon which was done by a short duration 25 sccm SF₆ plasma, followed by a short duration polymerization using 80 sccm C₄F₈. The passivation layer protected the entire substrate from further chemical attack and prevented further etching. Circular- and square-shaped pillars were fabricated according to the applied mask. The diameter, spacing and height of the pillars were 2 μm, 2 μm and 50 μm, respectively.

TiO₂ and Al₂O₃ ALD coatings: To investigate the coating effect, Si micropillars were coated with nanometer-thick Al₂O₃ or TiO₂ films using the well-established trimethyl-aluminum (AlMe₃/H₂O)^[18] and titanium tetrachloride (TiCl₄/H₂O)^[19] atomic layer deposition (ALD) processes in a warm wall reactor (wall temperature of 100 °C and stage temperature of 125 °C for Al₂O₃ and 110 °C for TiO₂). Growth of TiO₂ on a porous SiO₂ substrate via ALD under similar conditions has been demonstrated previously.^[20] Long pump, pulse and purge times (20s/50s/50s) were used to ensure uniform coatings throughout the material. The resulting film thicknesses using 15 cycles for TiO₂ and 3 cycles for Al₂O₃ are 1 nm and 0.75 nm, respectively.

Cell assembly and characterizations: The silicon micropillars standing on a Si wafer were directly assembled in a Swagelok-type half-cell (~71 mm² surface area) with metal lithium as both reference and counter electrodes. A commercial electrolyte (MTI Cor.) of 1 M LiPF₆ in a mixed solution of ethylene carbonate, diethyl carbonate and dimethyl carbonate (EC/DEC/DMC, v/v = 1:1:1) was adopted with a polypropylene separator (Celgard 3501, PP double layer, ~25 μm each). Cell assembly was conducted in Argon-filled glove box (VAC Omni) with oxygen and water content less than 1 ppm. A Maccor 4304 battery cycler was used to perform the lithiation process from the open circuit potential (~ 3 V) to a target voltage of 50 mV at a constant scan rate of 0.1 mV/s. The samples were first lithiated under a constant voltage scan rate of 0.1 mV/s from ~3 V to 50 mV, and then were held for 20 hrs. After electrochemical lithiation, cells were disassembled in the glove box and the lithiated electrodes were washed by dimethyl carbonate (DMC) for imaging analysis. The morphology change was characterized by a field-emission scanning electron microscope (SEM, JEOL 7401-F) operated at 2 kV.

Simulation Details

To understand quantitatively the effect of ALD coating and initial geometry on the VE and stress evolution of silicon micropillars upon lithiation, a two-phase model is adopted.^[21, 22] The model assumes that the rate-limiting processes during the lithiation involve the bulk diffusion of lithium ion through the pillars and the solid state reaction at the interface between phases (i.e., other rate-controlling mechanisms such as adsorption of Li on the surface of silicon pillars are ignored).^[23, 24] As all micropillars used in our experiments have very large aspect ratio (25:1), the effect of the pillar height can be neglected and a cross-section representation is sufficient enough to describe the VE behavior, the Cartesian coordinate setup of which can be seen in Fig. S5, with the origin coinciding with the geometric center of the cross-section and two axels along <110> directions. Coordinates (x,y), angle θ are used to specify positions and directions. The interface is a time dependent planar curve, as $F(x, y; t) = 0$. For the reaction controlled interface motion, interface velocity^[24] is determined by $v(\theta) = V_{Si} R$, with V_{Si} as the molar volume of crystalline silicon, and

$R = \kappa(\theta) f(c_{Li}, c_{Si}, c_{Li-Si})$, as the rate of chemical reaction, where $\kappa(\theta)$ is the orientation dependent rate constant for chemical reaction, and function $f(c_{Li}, c_{Si}, c_{Li-Si})$ describes the production rate as a function of the concentrations of products and reactants. Lithium concentration is assumed saturated in the amorphous phase and zero in the crystalline phase. Thus, function $f(c_{Li}, c_{Si}, c_{Li-Si})$ becomes a constant at the phase interface. Given the four fold symmetry of the crystal structure within the cross-section, the interface velocity can be described as

$$v(\theta) = \frac{1}{2}(v_{110} + v_{100}) + \frac{1}{2}(v_{110} - v_{100})\cos(4\theta).$$

Here $v_{110} = V_m f \kappa(0)$ and $v_{100} = V_m f \kappa(\pi/4)$ are the interface velocities at [110] and [100] orientations, respectively.

Finite deformation is considered in the modeling. The multiplicative decomposition of deformation is assumed so that the total deformation λ_i is decomposed into three parts, namely, elastic deformation λ_i^e , plastic deformation λ_i^p , and compositional deformation λ_i^c , as $\lambda_i = \lambda_i^e \lambda_i^p \lambda_i^c$. $i=1,2,3$ is used to denote the three principal directions, in which the compositional strain is given by $\lambda_i^c(x, y; t) = 1 + \beta c(x, y; t)$, with $c(x, y; t)$ as the normalized lithium concentration, β as the coefficient of compositional expansion. Elastic and plastic deformation are partitioned by the specific material law. Crystalline silicon is modeled as an cubic elastic material; amorphous Li-Si alloy and ALD coatings are both modeled as isotropic perfectly elastic-plastic materials. The von Mises yielding criterion and the associated flow rules are used to describe the plastic behavior of amorphous materials. Detailed formulation of equilibrium, compatibility, and constitutional models are available in the reference.^[25]

The model described above is implemented using the finite element package ABAQUS and two user-subroutines. We draw an analogy between concentration c in our problem and temperature in thermal analysis in ABAQUS. Therefore, a user subroutine UTEMP (user defined temperature) is used to explicitly evolve the interface according to the above equation with concentration $c=1$ assigned to the amorphous phase and $c=0$ to the crystalline phase. Another user subroutine UEXPAN is used to compute the compositional expansion based on the concentration field obtained from UTEMP, under rigorous finite deformation formulation. $\beta=0.5874$ is used to realize the 300% VE, as $(1+\beta)^3=1+300\%$. The field of compositional strain is passed into ABAQUS main program as the load to deform the electrode.

Table A lists the mechanical properties of materials involved in simulations. For ALD coatings, we choose Young's modulus $E=150$ GPa, hardness $H=8$ GPa^[26, 27], and Poisson's ratio $\nu=0.25$. For (100) crystalline silicon, $E=130$ GPa, Shear modulus $G=79.6$ GPa, and $\nu=0.28$.^[28, 29] For Si-Li amorphous phase, we choose $E=12$ GPa, $H=1.5$ GPa,^[30] and $\nu=0.28$. In the simulations, all length quantities are normalized by $a=1000$ nm, which in fact is the typical length around the size of the cross-section. $\tau=a/v_{110}$ is the time scale of fully lithiation; thus time is normalized by τ and velocity is normalized by τ/a , i.e., $\bar{v}_{110} = v_{110}\tau/a$, $\bar{v}_{100} = v_{100}\tau/a$. For bare pillars and ALD coated pillars, the same velocity in 110 orientation was used as $\bar{v}_{110}=1$ while different values $\bar{v}_{100}=0.9$ and $\bar{v}_{100}=0.6$ were used respectively to recognize the different levels of the anisotropy in those two kinds of samples. ALD coatings itself was modeled as a thin layer of material with a thickness of 0.005.

Table A. Representative mechanical properties of some relevant materials from the literature

Materials	Mechanical Properties
Amorphous TiO ₂	E=65~147 GPa ^[27]
Amorphous Al ₂ O ₃	E=150-155 GPa, H=8 GPa ^[26]
Amorphous Li ₁₅ Si ₄	E=12 GPa, H=1.5 GPa ^[30]
Single crystalline Si (100)	E=130 GPa, G=79.6 GPa, ν =0.28 ^[28, 29]

*E- Young's Modulus, ν - Poisson's Ratio, H- Hardness, G- Shear Modulus

Supporting Information

Supporting Information is available online from the Wiley Online Library or from the author.

Acknowledgements

The authors would like to thank C.E. Reinhardt for experimental assistance. Helpful discussions with B.C. Wood, T.W. Heo, J. Lee and M.D. Merrill are acknowledged. The work was performed under the auspices of the US Department of Energy by LLNL under contract No. DE-AC52-07NA27344. The project is supported by the Laboratory Directed Research and Development (LDRD) programs of LLNL (12-ERD-053 and 13-LW-031).

Received: ((will be filled in by the editorial staff))

Revised: ((will be filled in by the editorial staff))

Published online: ((will be filled in by the editorial staff))

- [1] H. Wu, G. Chan, J. W. Choi, I. Ryu, Y. Yao, M. T. McDowell, S. W. Lee, A. Jackson, Y. Yang, L. B. Hu, Y. Cui, *Nature Nanotech.* **2012**, 7, 309.
- [2] X. H. Liu, J. W. Wang, S. Huang, F. F. Fan, X. Huang, Y. Liu, S. Krylyuk, J. Yoo, S. A. Dayeh, A. V. Davydov, S. X. Mao, S. T. Picraux, S. L. Zhang, J. Li, T. Zhu, J. Y. Huang, *Nature Nanotech.* **2012**, 7, 749.
- [3] S. W. Lee, M. T. McDowell, L. A. Berla, W. D. Nix, Y. Cui, *Proc. Natl. Acad. Sci. U. S. A.* **2012**, 109, 4080.
- [4] H. Kim, B. Han, J. Choo, J. Cho, *Angew. Chem. Int. Ed. Engl.* **2008**, 47, 10151.
- [5] J. K. Yoo, J. Kim, Y. S. Jung, K. Kang, *Adv. Mater.* **2012**, 24, 5452.
- [6] M. H. Ryou, J. Kim, I. Lee, S. Kim, Y. K. Jeong, S. Hong, J. H. Ryu, T. S. Kim, J. K. Park, H. Lee, J. W. Choi, *Adv. Mater.* **2013**, 25, 1571.
- [7] C. J. Yu, X. Li, T. Ma, J. P. Rong, R. J. Zhang, J. Shaffer, Y. H. An, Q. Liu, B. Q. Wei, H. Q. Jiang, *Adv. Energy Mater.* **2012**, 2, 68.
- [8] S. B. Son, S. C. Kim, C. S. Kang, T. A. Yersak, Y. C. Kim, C. G. Lee, S. H. Moon, J. S. Cho, J. T. Moon, K. H. Oh, S. H. Lee, *Adv. Energy Mater.* **2012**, 2, 1226.
- [9] J. W. Wang, Y. He, F. F. Fan, X. H. Liu, S. M. Xia, Y. Liu, C. T. Harris, H. Li, J. Y. Huang, S. X. Mao, T. Zhu, *Nano Lett.* **2013**, 13, 709.
- [10] J. L. Goldman, B. R. Long, A. A. Gewirth, R. G. Nuzzo, *Adv. Funct. Mater.* **2011**, 21, 2412.
- [11] R. Yi, F. Dai, M. L. Gordin, S. R. Chen, D. H. Wang, *Adv. Energy Mater.* **2013**, 3, 295.
- [12] C. K. Chan, R. Ruffo, S. S. Hong, Y. Cui, *J. Power Sources* **2009**, 189, 1132.

- [13] X. C. Xiao, P. Lu, D. Ahn, *Adv. Mater.* **2011**, 23, 3911.
- [14] Y. He, X. Q. Yu, Y. H. Wang, H. Li, X. J. Huang, *Adv. Mater.* **2011**, 23, 4938.
- [15] Q. Shao, L. F. Voss, A. M. Conway, R. J. Nikolic, M. A. Dar, C. L. Cheung, *Appl. Phys. Lett.* **2013**, 102, 063505.
- [16] X. H. Liu, H. Zheng, L. Zhong, S. Huan, K. Karki, L. Q. Zhang, Y. Liu, A. Kushima, W. T. Liang, J. W. Wang, J. H. Cho, E. Epstein, S. A. Dayeh, S. T. Picraux, T. Zhu, J. Li, J. P. Sullivan, J. Cumings, C. S. Wang, S. X. Mao, Z. Z. Ye, S. L. Zhang, J. Y. Huang, *Nano Lett.* **2011**, 11, 3312.
- [17] H. Yang, S. Huang, X. Huang, F. F. Fan, W. T. Liang, X. H. Liu, L. Q. Chen, J. Y. Huang, J. Li, T. Zhu, S. L. Zhang, *Nano Lett.* **2012**, 12, 1953.
- [18] S. M. George, *Chem. Rev.* **2010**, 110, 111.
- [19] J. Aarik, A. Aidla, H. Mandar, T. Uustare, *Appl. Surf. Sci.* **2001**, 172, 148.
- [20] S. Ghosal, T. F. Baumann, J. S. King, S. O. Kucheyev, Y. M. Wang, M. A. Worsley, J. Biener, S. F. Bent, A. V. Hamza, *Chem. Mater.* **2009**, 21, 1989.
- [21] P. Limthongkul, Y. I. Jang, N. J. Dudney, Y. M. Chiang, *Acta Mater.* **2003**, 51, 1103.
- [22] X. H. Liu, L. Q. Zhang, L. Zhong, Y. Liu, H. Zheng, J. W. Wang, J. H. Cho, S. A. Dayeh, S. T. Picraux, J. P. Sullivan, S. X. Mao, Z. Z. Ye, J. Y. Huang, *Nano Lett.* **2011**, 11, 2251.
- [23] U. Gosele, K. N. Tu, *J. Appl. Phys.* **1982**, 53, 3252.
- [24] Z. W. Cui, F. Gao, J. M. Qu, *J. Mech. Phys. Solids* **2013**, 61, 293.
- [25] K. J. Zhao, M. Pharr, S. Q. Cai, J. J. Vlassak, Z. G. Suo, *J. Am. Ceram. Soc.* **2011**, 94, S226.
- [26] C. F. Herrmann, F. W. DelRio, S. M. George, V. M. Bright, **2005**, 159.
- [27] O. Anderson, C. R. Ottermann, R. Kuschnerit, P. Hess, K. Bange, *Fresenius' J. Analy. Chem.* **1997**, 358, 290.
- [28] M. A. Hopcroft, W. D. Nix, T. W. Kenny, *J. MEMS* **2010**, 19, 229.
- [29] J. J. Wortman, R. A. Evans, *J. Appl. Phys.* **1965**, 36, 153.
- [30] B. Hertzberg, J. Benson, G. Yushin, *Electrochem. Commun.* **2011**, 13, 818.

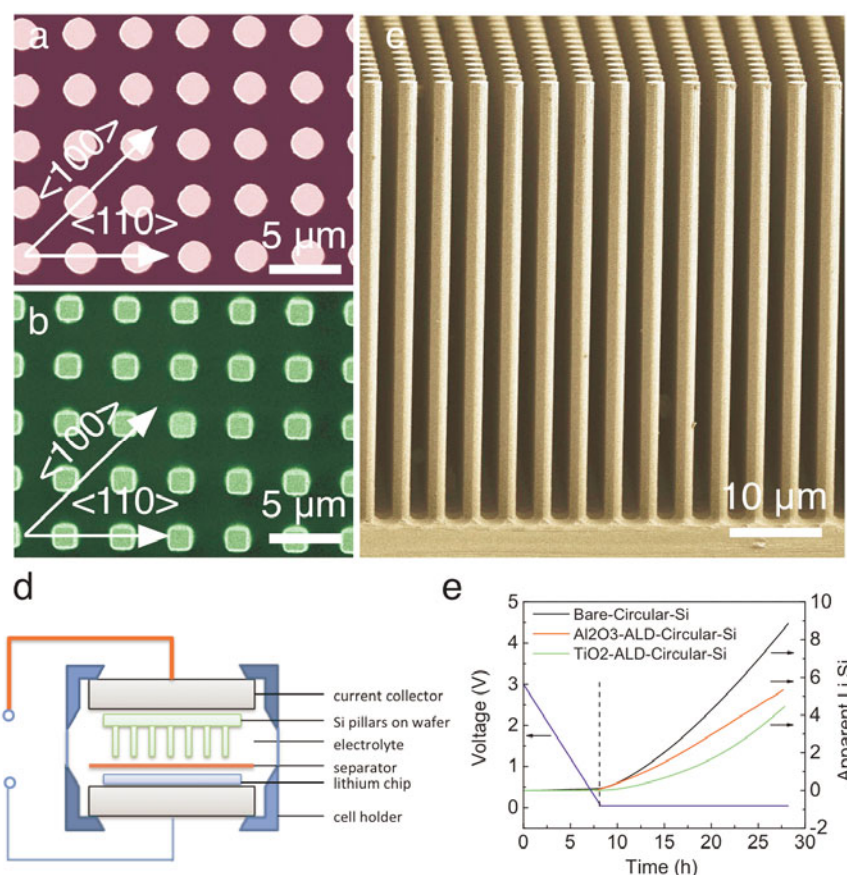


Figure 1. Initial morphology of silicon micropillars and the experimental setup. (a) and (b), top-view scanning electron micrograph (SEM) of circular and square pillars, respectively. The crystallographic orientations are labeled in the figure. (c) A side-view SEM image of circular pillars. (d) An illustration of our experimental setup using a half-cell assembly. (e) Voltage and lithiation profile of three types of circular pillars. Note that the apparent lithiation rate of ALD-coated samples seems lower compared to the bare-Circular-Si. This phenomenon could be caused by the formation of massive SEI layers without ALD coatings (see text for detailed discussion).

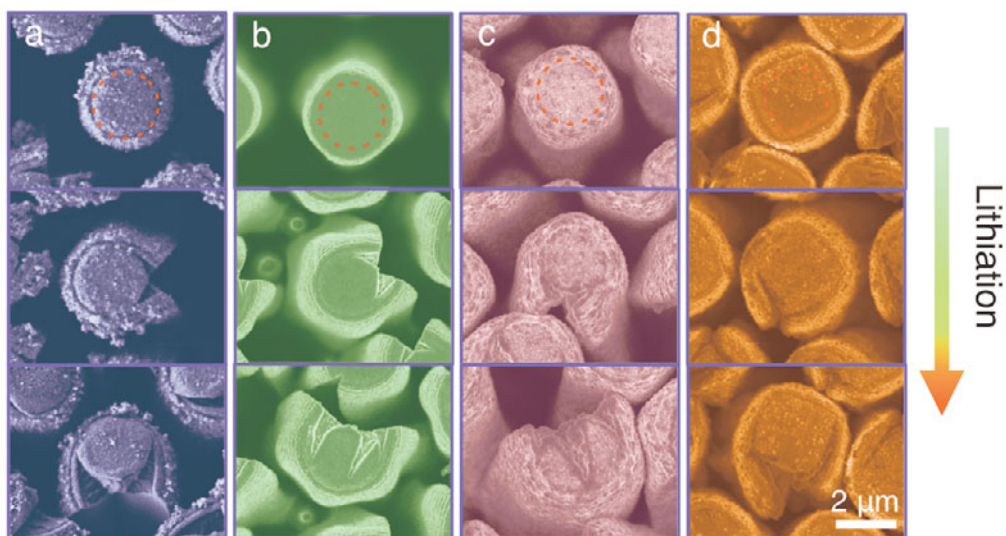


Figure 2. Cross-sectional morphology evolutions during the lithiation for four types of silicon pillars: (a) bare-Circular-Si, (b) Al_2O_3 -ALD-Circular-Si, (c) TiO_2 -ALD-Circular-Si, and (d) TiO_2 -ALD-Square-Si. The red dashed lines in the first row denote the original size and shape of the respective pillars. All images have the same scale bar. Note the very different shape change and fracture patterns/directions in these pillars.

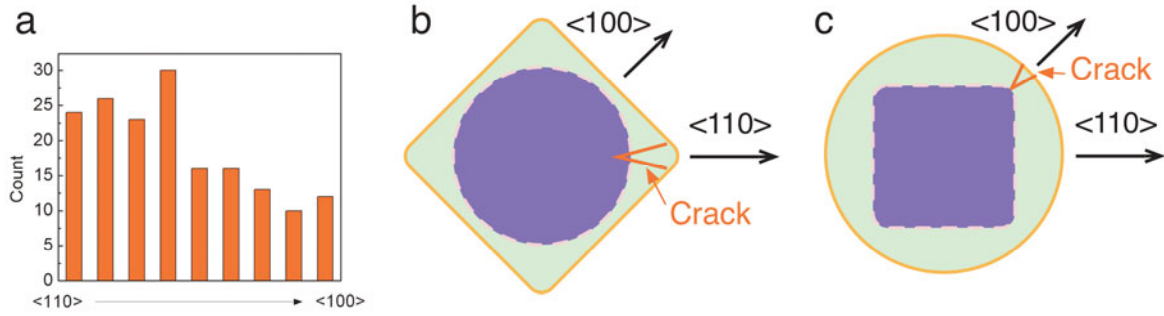


Figure 3. Crack orientations for three types of silicon pillars: (a) bare-Circular-Si, (b) ALD-Circular-Si (for both Al_2O_3 and TiO_2 coated), and (c) TiO_2 -ALD-Square-Si. Note that all ALD-coated pillars ubiquitously fail along one orientation [either $\langle 110 \rangle$ in (b), or $\langle 100 \rangle$ in (c)], in contrast to the relatively random failure direction of bare silicon sample in (a).

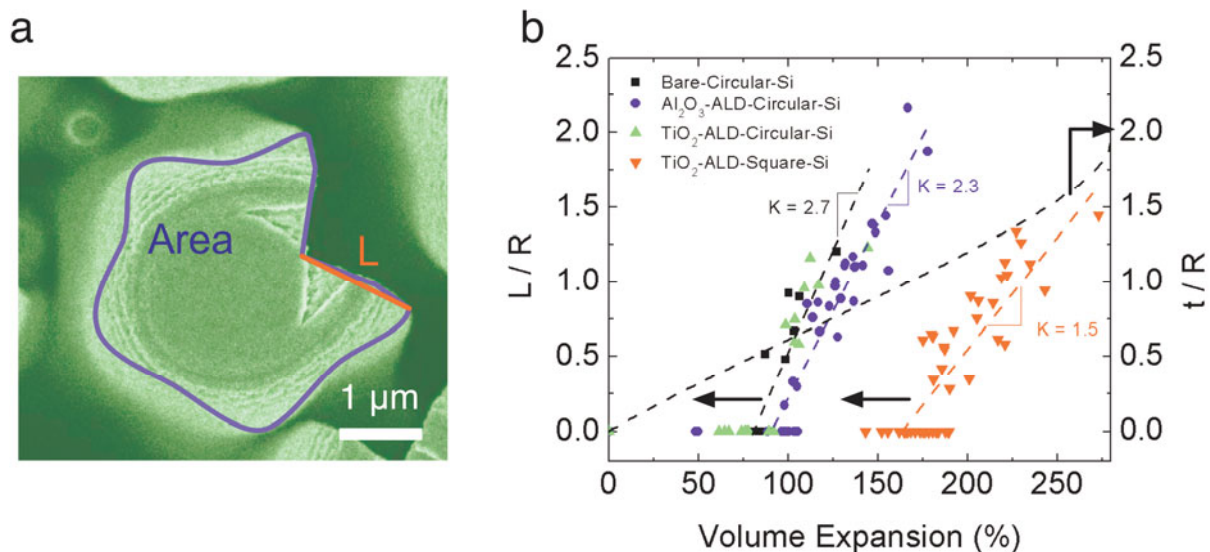


Figure 4. Crack nucleation and growth behavior in four types of silicon pillars. (a) The definition of L (crack length) and R (original pillar radius). The ΔV is measured by the change of pillar area on top-view using the ImageJ software. The amorphous shell thickness t is estimated according to eqn. 1 in the main text. (b) The distribution of L/R (y1-axis) and t/R (y2-axis) as a function of the VE. Three L/R dashed lines are the least-squares-fitting of the experimental data with the slope (K) marked in the figure.

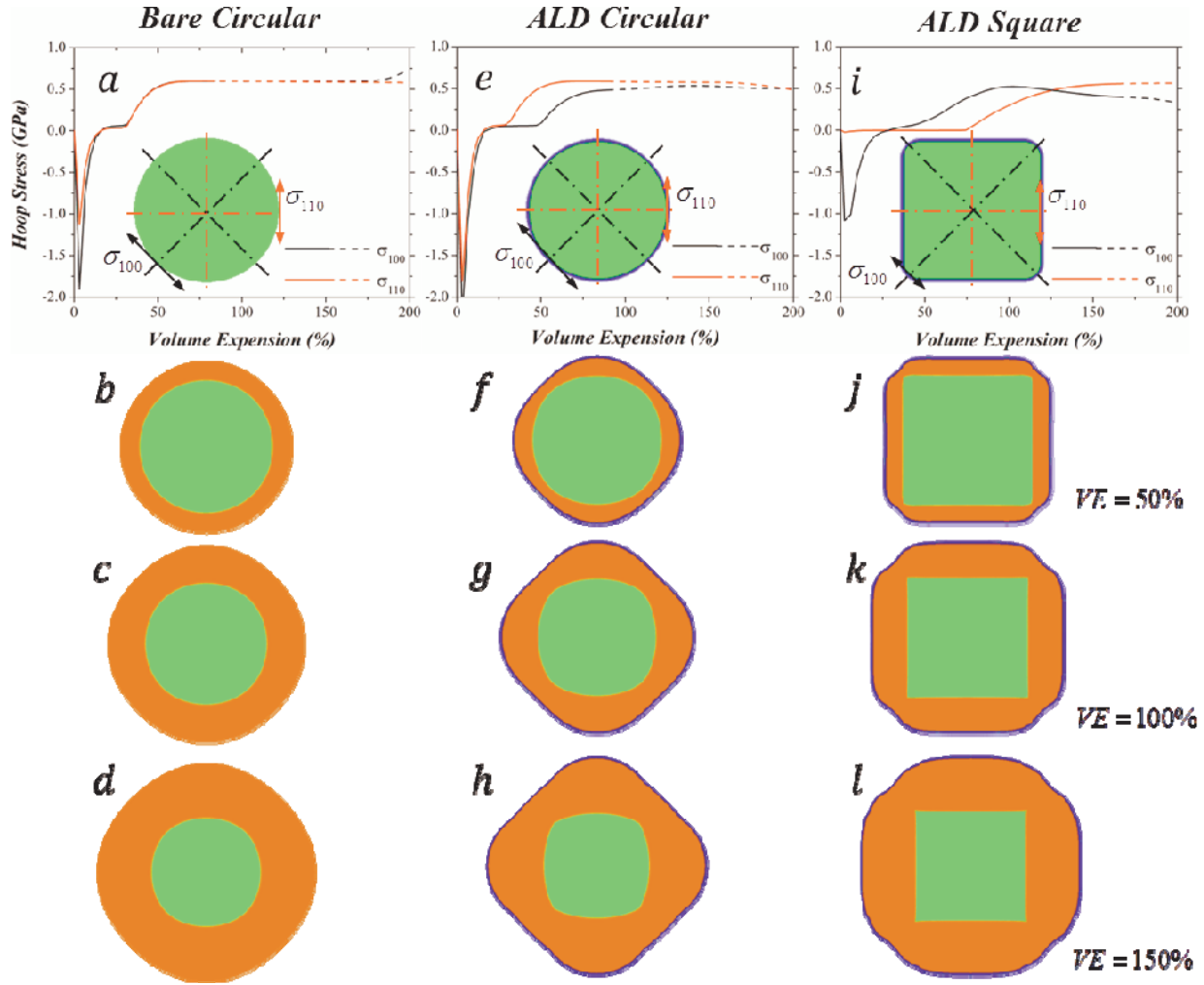


Figure 5. Finite element simulation results for (a-d) bare-Circular-Si, (e-h) ALD-coated circular pillars, and (i-l) ALD-coated square pillars. (a) Hoop stress as a function of VE at the surface of the bare-Circular-Si perpendicular to $\langle 100 \rangle$ (black line) and $\langle 110 \rangle$ (red line) directions, respectively. (b-d). The shape change in cross-section of the bare-Circular-Si, with crystalline Si in green and amorphous Li-Si in orange at different VE of 50%, 100%, 150%, respectively. The definition of hoop stress and shape change in (e-h) and (i-l) follows the same order as the bare-Circular-Si. Note the rather anisotropic expansion behavior after ALD-coating for circular pillars (f-h), and the near circle-like expansion behavior of the square pillars (j-l). The ALD thin coating in (f-h) and (j-l) is represented by the blue solid line.

Table 1. Anisotropic shape index before (χ_{before}) and after (χ_{after}) lithiation for various silicon pillars, which is defined as the ratio of dimension along $\langle 110 \rangle$ and $\langle 100 \rangle$ directions: $\chi = d_{\langle 110 \rangle} / d_{\langle 100 \rangle}$. χ_{after} is measured at ΔV_c (the maximum volume expansion before the crack formation).

Pillar type	Geometry	χ_{before}	χ_{after}
Bare-Circular-Si		1	1.02 ± 0.03 @ $\Delta V_c^{\text{b)}} = 82\%$
Al ₂ O ₃ -ALD-Circular-Si		1	1.15 ± 0.03 @ $\Delta V_c = 92\%$
TiO ₂ -ALD-Circular-Si		1	1.13 ± 0.04 @ $\Delta V_c = 88\%$
TiO ₂ -ALD-Square-Si		0.71	0.95 ± 0.02 @ $\Delta V_c = 165\%$

The table of contents entry

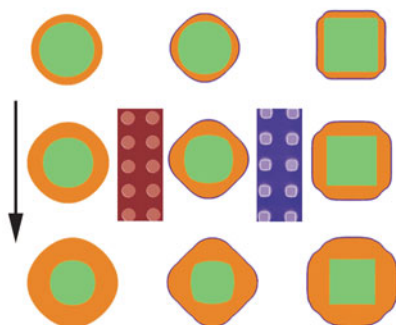
Lithiation of large aspect-ratio (~ 25), well-patterned (100) silicon circular pillars ($\sim 2\mu\text{m}$ in diameter) with and without atomic layer deposited thin metal oxides (Al_2O_3 and TiO_2) reveals drastically different volume expansion anisotropy and fracture patterns. Geometry studies reveal that square-pillars exhibit nearly twice volume expansion without fracture. Mechanisms of various failure modes are discussed, based upon our own modeling effort.

Keyword (see list)

*Jianchao Ye, Yonghao An, Monika M. Biener, Rebecca J. Nikolic, Ming Tang, Hanqing Jiang, Y. Morris Wang**

Title: Unusual lithiation and fracture behavior of silicon mesoscale pillars: roles of ultrathin atomic layer coating and initial geometry

ToC figure (55 mm \times 50 mm)



Supporting Information

for *Adv. Energy Mater.*, DOI: 10.1002/aenm.((please add manuscript number))

Unusual lithiation and fracture behavior of silicon mesoscale pillars: roles of ultrathin atomic layer coatings and initial geometry

*Jianchao Ye, Yonghao An, Monika M. Biener, Rebecca J. Nikolic, Ming Tang, Hangqing Jiang, Y. Morris Wang**

Dr. J.C. Ye, Y.H. An, Dr. M.M. Biener, Dr. M. Tang, Dr. Y.M. Wang^{*}
Physical and Life Sciences Directorate, Lawrence Livermore National Laboratory, Livermore,
CA 94550, USA
Email: ymwang@llnl.gov

Dr. R.J. Nikolic
Center for Micro and Nano Technology, Lawrence Livermore National Laboratory,
Livermore, CA 94550, USA

Y.H. An, Prof. H. Jiang
School for Engineering of Matter Transport and Energy, Arizona State University, Tempe,
AZ 85287, USA

Table S1. Some physical properties of silicon, SiO₂ and metal oxides

Materials	Fracture toughness (MPa m^{1/2})	Electrical conductivity (S/cm)	Li ion conductivity (S/cm)
Al₂O₃	2.7 - 4.2 ^[1]	10 ⁻¹⁴ ^[2] (crystalline)	10 ⁻⁶ ^[3] (amorphous)
TiO₂	2.38 ^[1]	10 ⁻⁶ ^[4]	10 ⁻⁵ - 10 ⁻⁷ ^[5] (Rutile)
SiO₂	0.79	10 ⁻¹⁴	-
Si	<110>: 0.73 <100>: 0.89 ^[6]	2 (our work)	~3 × 10 ⁻⁷ ^[7]

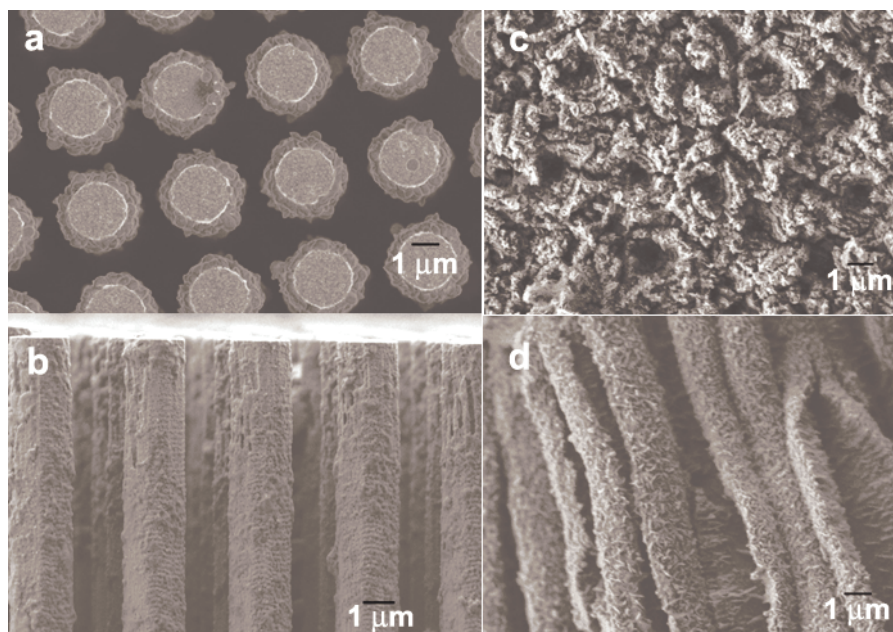


Figure S1. Micrographs of the bare-circular-Si after partial (120 mV, 20 hrs) and full lithiation (10 mV, 20 hrs). (a) and (b), top- and side-view of a partially lithiated bare Si sample. Note the very thick solid electrolyte interphase (SEI) layers and uniform expansion behavior in (a). (c) and (d), top- and side-view of the fully lithiated bare Si.

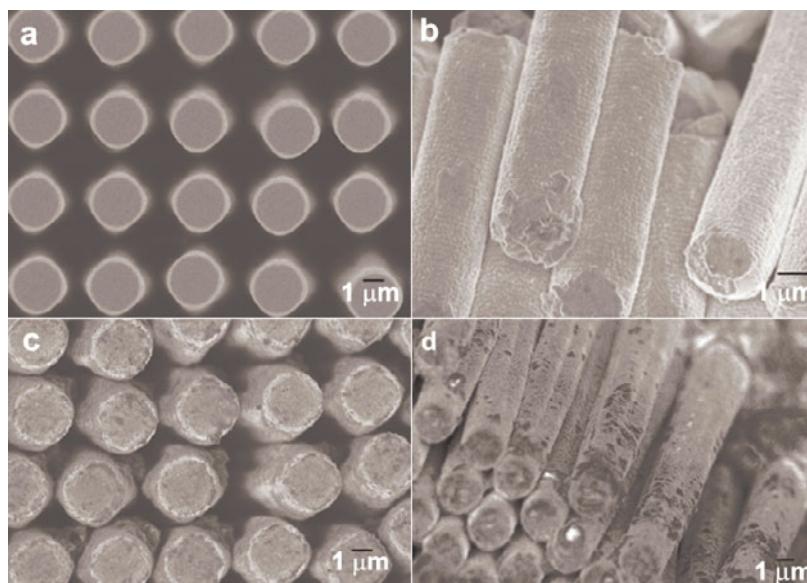


Figure S2. Micrographs of partially lithiated ALD-coated samples. (a) and (b), top- and side-view of Al₂O₃-ALD-Circular-Si after partial lithiation. Note the very clean surface nature of this sample. (c) and (d), top- and side-view of TiO₂-ALD-Circular-Si after partial lithiation.

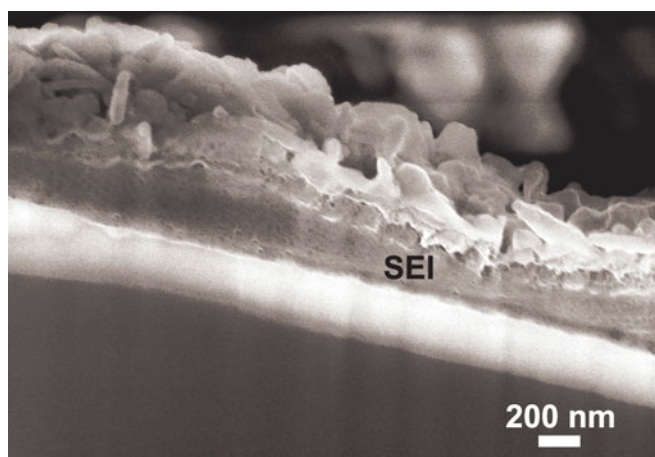


Figure S3. Focused-ion-beam (FIB) cross-sectional cutting of Al₂O₃-ALD-Circular-Si sample after partial lithiation. Note that the sample was exposed to the air for more than 48 hrs before the FIB sectioning, which may have substantially increased the surface roughness of the SEI layer (compare Fig. S3 to Fig. S2b).

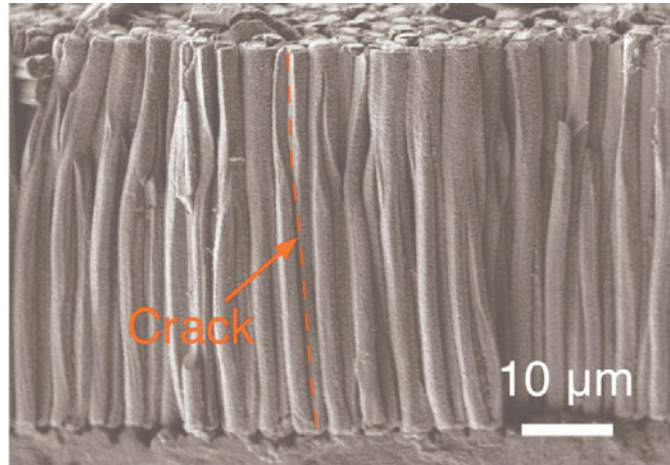


Figure S4. The cross sectional SEM image of the fractured bare circular silicon micropillars, indicating the height change of the pillars is negligibly small compared to the cross-section expansion. The fracture is also found throughout the pillars.

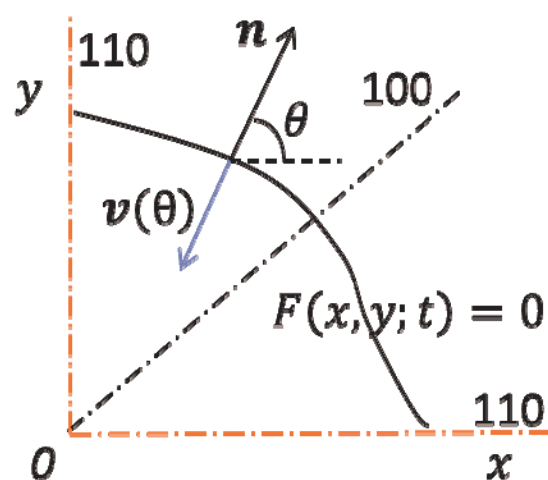


Figure S5. Illustration of coordinate system setup used in the finite element simulations.

References for Supporting Information

- [1] J. Cho, Y. J. Kim, T. J. Kim, B. Park, *Angew. Chem. Int. Ed.* **2001**, 40, 3367.
- [2] G. V. Samsonov, *The Oxide Handbook*, IFI/Plenum, New York 1982.
- [3] A. M. Glass, K. Nassau, *J. Appl. Phys.* **1980**, 51, 3756.
- [4] L. F. Shen, X. G. Zhang, H. S. Li, C. Z. Yuan, G. Z. Cao, *J. Phys. Chem. Lett.* **2011**, 2, 3096.
- [5] H. Yildirim, J. P. Greeley, S. K. R. S. Sankaranarayanan, *PCCP* **2012**, 14, 4565.
- [6] M. TANAKA, K. HIGASHIDA, H. NAKASHIMA, H. TAKAGI, M. FUJIWARA, *Int. J. Fracture* **2006**, 139, 383.
- [7] N. Ding, J. Xu, Y. X. Yao, G. Wegner, X. Fang, C. H. Chen, I. Lieberwirth, *Solid State Ionics* **2009**, 180, 222.